Available online at www.sciencedirect.com

jmr&t Journal of Materials Research and Technology

journal homepage: www.elsevier.com/locate/jmrt

Optimization of processing parameters and microstructure evolution of (TiB+La_2O_3)/Ti6Al4V manufactured by laser melting deposition

Yuyu Liu [a,b], Wei Jiang [a], Zheng Chen [a,**], Quan Xu [a], Zhiliang Zhang [b], Jianying He [b,*]

[a] School of Material Science and Engineering, China University of Mining and Technology, Xuzhou 221116, China
[b] Department of Structural Engineering, Norwegian University of Science and Technology, Trondheim 7491, Norway

ARTICLE INFO

Article history:
Received 26 January 2023
Accepted 5 May 2023
Available online 9 May 2023

Keywords:
Laser melting deposition
Titanium matrix composites
Parameter optimization
Microstructure evolution
Fracture

ABSTRACT

Due to the intrinsically ultrahigh cooling rate and thermal gradient during laser melting deposition (LMD), columnar-to-equiaxed transition (CET) of grains has been a significant challenge in titanium-based alloys. In this study, two strategies, including the optimization of processing parameters and the addition of ceramics particles, were utilized to promote the CET of Ti6Al4V. The optimal processing parameters of Ti6Al4V were confirmed by response surface methodology (RSM). The width of prior β grains effectively decreases under the minimum dilution of single track. Besides, different contents of TiB_2 and La_2O_3 were added to Ti6Al4V powder and the in situ (TiB + La_2O_3)/Ti6Al4V composites were manufactured using the identified optimal processing parameters. In situ TiB whiskers segregating at the grain boundaries tailor the coarse columnar to equiaxed grains with La_2O_3 particles dispersed in the composites. With increasing formation of the reinforcements, equiaxed grain size decreases from 23.3 to 11.9 μm. The ultimate tensile strength of the components was improved by 19.6% and 26.4% compared to that of Ti6Al4V. This work provides systematic solutions to suppress the coarse columnar grains and refine the microstructure for titanium-based alloys.

1. Introduction

Laser melting deposition (LMD) is one of additive manufacturing (AM) processes, in which components are built laser-by-laser via coaxial laser scanning and powder feeding [1,2]. This process is characterized by high flexibility, accuracy, and near-net shape, suitable for the fabrication of titanium-based alloys. However, metallic materials, especially titanium-based alloys, manufactured by AM technologies generally suffer from undesirable coarse columnar grains that result in anisotropic mechanical properties [3–5]. There are two dominant grain growth behaviors during the solidification of LMD, including the heterogenous nucleation for equiaxed grains and epitaxial growth for columnar grains [6]. Attempts to optimize the processing parameters of LMD and introduce ceramics as nucleating agents have been made to promote columnar to equiaxed transition (CET) [7–10].

* Corresponding author.
** Corresponding author.
E-mail addresses: chenzheng1218@163.com (Z. Chen), jianying.he@ntnu.no (J. He).
https://doi.org/10.1016/j.jmrt.2023.05.058

During LMD, the single laser track of the multiple-layer depositions is controlled by three main processing parameters including laser power (*P*), feed rate (*f*), and scanning speed (*v*). The various combinations of the parameters determine the geometry and quality of the track. However, the printing parameters are generally designed by empirical choice. Dilution is a significant factor for the deposited layer, representing the extent of mixing between the clad material and the base material, which can figure out an appropriate range of the parameter [11]. It reported that the dilution of a clad layer is defined as the ratio of cladding depth to the sum of its height and depth [12]. To avoid the excessive melting of the prior track during AM process, the ratio should be moderately small. Large dilution generally leads to high melt superheating, large penetration re-melting, and epitaxial growth. The equiaxed grains were finally obtained under a superhigh feed rate [13]. Therefore, choosing suitable processing parameters is of vital importance during LMD.

Besides optimizing the processing parameter, the addition of ceramics is also an effective approach for titanium alloy to achieve equiaxed grains and improve mechanical performance. Huang et al. [14] reported that the addition can be divided into ex-situ and in-situ techniques depending on the different forms of reinforcement. For the ex-situ method, the added reinforcement powders or tiny particles are unable to react with the titanium matrix and exhibit a homogeneous discrete distribution, such as TiB, TiC, TiN [15], and Ti_5Si_3 [16]. In contrast, in-situ reinforcements are attributed to the reaction between the titanium matrix and added compound, such as TiB_2 [17], B_4C [8], and SiC [18]. In-situ reinforcements are expected to exhibit chemical stability and compatibility with the matrix. Pouzet et al. [19] blended B_4C and Ti6Al4V powders to manufacture (TiB + TiC)/Ti6Al4V alloys by direct metal deposition due to the in-situ chemical reaction $5Ti + B_4C \rightarrow 4TiB + TiC$. Hu et al. [20] reported that TiB_2 reinforcements were added to obtain TiB/Ti composites using the in-situ laser deposition process according to in-situ reaction $TiB_2 + Ti \rightarrow 2TiB$. The yield strength of the TiB/Ti was enhanced with the increased aspect ratio of TiB and decreased TiB whisker size. Among the reinforcements, the in-situ TiB whisker is one of the most suitable reinforcements for the titanium alloys. Tjong et al. [21] proposed three advantages of in-situ reaction compared to the ex-situ process. In-situ TiB is thermodynamically stable at the matrix with no intermediate between TiB and titanium. The in-situ process is beneficial to obtain a clean interface that results in a strong metallurgical bonding. Finally, TiB and Ti share similar densities (4.51 and 4.54 g/cm^3, respectively) and a small thermal expansion coefficient difference [22]. The distribution of TiB in the matrix is more uniform, yielding better mechanical properties. Besides, Bermingham et al. [23] used La_2O_3 as nucleation particles to refine titanium alloys by wire and arc additive manufacturing (WAAM) and equiaxed grain formation is achieved due to β-Ti nucleation on La_2O_3.

In the study, TiB_2 and La_2O_3 were chosen as coupling agents for Ti6Al4V to promote the CET by in-situ synthesis of LMD. The geometry data of single tracks were collected to determine the optimal processing parameters with the aim of minimum dilution. The influence of the in-situ reinforcements on the microstructure and phase evolution of Ti6Al4V was also revealed. The orientation of in-situ TiB and La_2O_3 between titanium matrix was investigated to explain the grain refining effect. The mechanical properties of in-situ (TiB + La_2O_3)/Ti6Al4V composites were tested for comparison with Ti6Al4V.

2. Materials and methods

2.1. Optimization of processing parameter

The raw material of Ti6Al4V powder was purchased from Hangtian Haiying Co Ltd. Fig. 1a shows the nearly spherical

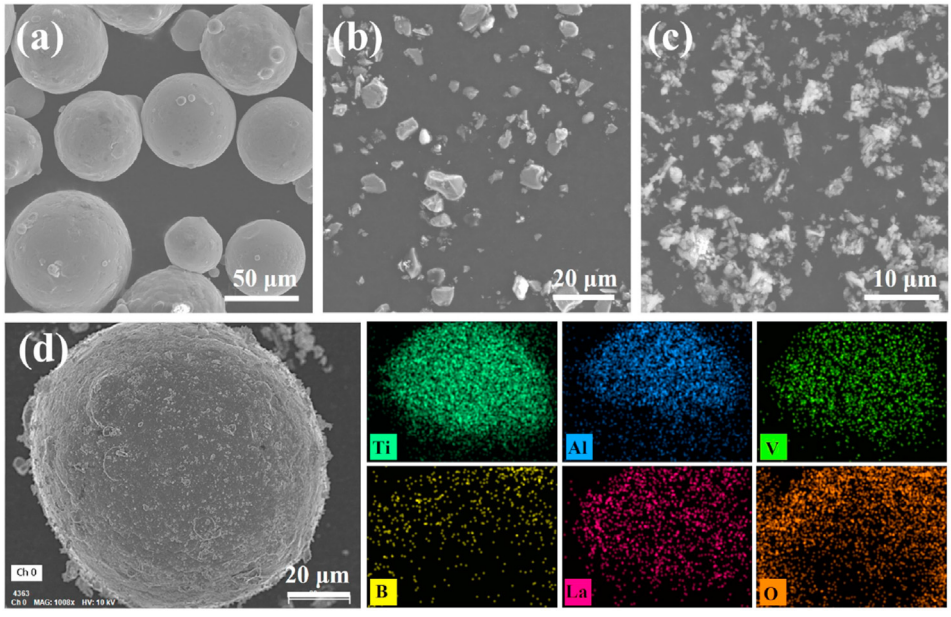

Fig. 1 – (a) Raw Ti6Al4V powder with the nearly spherical shape; (b) TiB_2 particles; (c) La_2O_3 particles; (d) the blended Ti6Al4V powder enclosed by TiB_2 and La_2O_3 with EDS mapping for feeding during LMD process.

Table 1 – Independent parameters and responses of CCD RSM process. (Std. Order: Standard order.)

Std. order	Run order	Parameters			Response			
		P (W)	*v* (mm/min)	*f* (g/min)	*w* (mm)	*h* (mm)	*d* (mm)	*Dilution*
3	1	1200	480	3.6	2.830	0.121	0.408	0.771
18	2	1200	600	3.6	2.684	0.133	0.400	0.750
10	3	1500	480	3.6	3.469	0.233	0.502	0.683
7	4	1200	360	4.8	3.025	0.251	0.489	0.661
19	5	1800	480	3.6	3.843	0.209	0.609	0.745
5	6	1800	480	4.8	4.046	0.182	0.500	0.733
6	7	1800	600	4.8	3.646	0.232	0.543	0.700
14	8	1200	360	6	3.009	0.370	0.560	0.602
2	9	1800	600	6	4.231	0.159	0.462	0.744
8	10	1200	480	4.8	2.934	0.154	0.473	0.736
17	11	1200	360	3.6	3.018	0.177	0.430	0.708
9	12	1500	360	4.8	3.651	0.383	0.648	0.628
12	13	1500	600	6	3.263	0.177	0.456	0.720
16	14	1500	360	3.6	3.750	0.209	0.527	0.716
4	15	1500	480	4.8	3.451	0.185	0.422	0.695
20	16	1800	480	6	3.860	0.390	0.724	0.676
15	17	1500	600	3.6	3.251	0.179	0.428	0.705
13	18	1800	360	3.6	4.345	0.200	0.663	0.768
1	19	1500	600	4.8	3.217	0.246	0.524	0.681
11	20	1200	600	6	2.800	0.141	0.401	0.740

shape Ti6Al4V powder with the diameter of 50–150 μm. The powders were kept in vacuum at 80 °C, 6 h for drying. The LMD machine was equipped with the ytterbium fiber laser (wavelength of 1.07 μm, beam diameter of 3 mm), powder and shield gas delivery, printing chamber, and computational control systems. To prevent oxidization, the oxygen content was kept under 200 ppm during the fabrication. Ti6Al4V powder was deposited on the substrate (Ti6Al4V) to obtain 20 single tracks under the different combinations of processing parameters. The ranges of parameters for laser power (*P*), scanning speed (*v*), and feed rate (*f*) were 1200–1800 W, 360–480 mm/min, and 3.6–6.0 g/min. Different combinations of parameters are shown in Table 1.

The cross-section geometries with width (*w*), height (*h*), and depth (*d*) were observed in Fig. 2, and the dilution was calculated as dilution $= d/(d + h)$ [11,12]. The experimental data of the tracks were analyzed by the central composite design (CCD) of response surface methodology (RSM). The optimal parameters were obtained by Minitab software and applied to the subsequent fabrication of Ti6Al4V during LMD.

2.2. Addition of ceramic to Ti6Al4V for feeding

TiB_2 and La_2O_3 powders purchased from Aladdin Industrial Corporation were chosen as nucleating agents. Fig. 1b shows the added TiB_2 with the fine irregular polygon shape in size range 4–8 μm. Fig. 1c shows La_2O_3 particles with the size of 2–5 μm. Three samples with pure Ti6Al4V, (3 wt% TiB_2+0.5 wt % La_2O_3)/Ti6Al4V, and (5 wt% TiB_2+0.5 wt% La_2O_3)/Ti6Al4V were denoted as TMC0, TMC1, and TMC2. Before the LMD process, all the raw powders were also kept in vacuum at 80 °C, 6 h for drying. Ti6Al4V and two ceramic powders were mechanically mixed in a blender for 6 h to make Ti6Al4V spheres homogeneously covered by TiB_2 and La_2O_3. Fig. 1d and EDS mapping indicate that the pre-treated powder remains spherical and well-enclosed for feeding during the LMD process. The processing parameters were chosen from the optimization of single tracks. Two kinds of S-shaped scanning paths were used and the scanning directions between the successive paths were vertical.

2.3. Materials characterization

The cross-section samples along the building direction were first polished by 0.05 μm colloidal silica and etched by Kroll's reagent (10% HF, 20% HNO_3, 70% H_2O) for 15 s. The microstructure of samples was observed by optical microscope (OM, Olympus-PMG3) and scanning electron microscope (SEM, Hitachi SU8220) equipped with energy dispersive spectrometry (EDS, Bruker, QUANTAX). The lattice structures were identified by X-ray diffractometry (XRD, Bruker D8 Advance). Transmission electron microscopy (TEM, JEM 2100 Microscope) with the selected area electron diffraction (SAED) patterns were operated at a 200 kV operating voltage to characterize titanium and reinforcements.

As-printed samples with a dog-bone shape from TMC0, TMC1, and TMC2 were prepared through cutting, grinding, and polishing. The tensile testing was performed by the universal tensile tester (INSTRON 3382) at a strain rate of 10^{-3} s^{-1}.

3. 3. confirmation of the optimal parameter combination

3.1. RSM for single tracks

Fig. 2 shows the geometries of 20 single tracks with different processing parameters and the data are collected in Table 1. The corresponding dilution is calculated and listed in Table 1. The parameters of *P*, *v*, and *f* are used as interdependent

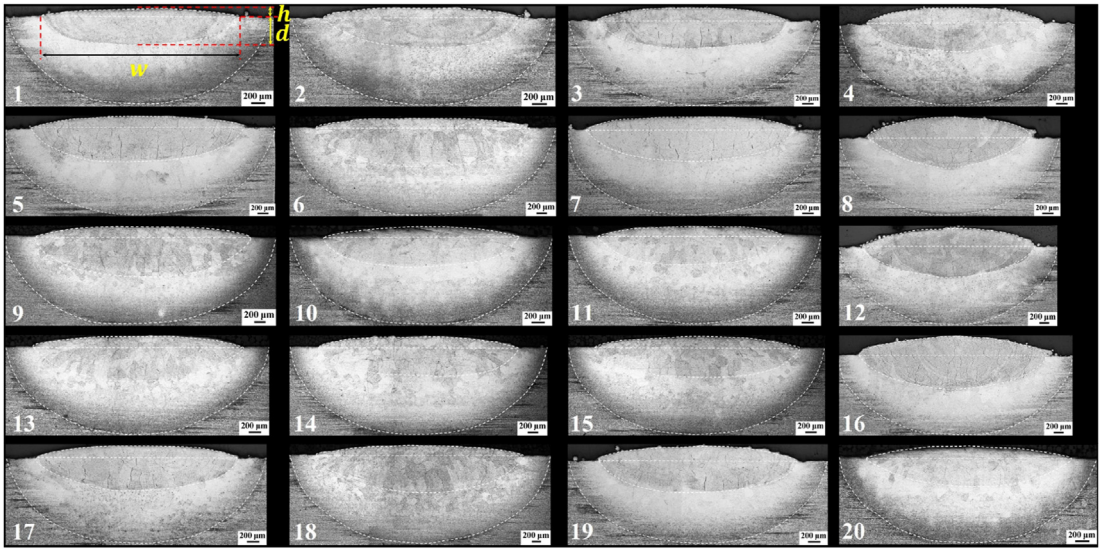

Fig. 2 – Cross-section geometries of 20 single tracks under different deposited parameters. The geometries of *h*, *d*, and *w* are displayed in first single track.

responses, and dilution as dependent responses, to obtain the optimal parameters. RSM is used to build the relationship between the processing parameters and the dilution.

The second-order regression is shown in a polynomial equation, as reported by Chelladurai et al. [24]:

$$S = a_0 + \sum_{i=1}^{k} a_i x_j + \sum_{i=1}^{k} a_{ii} x_i^2 + \sum_{i,j=1, j\neq i}^{k} a_{ij} x_i x_j + \varepsilon \quad (1)$$

where S is the predicted response, a_0 is a constant, a_i, a_{ii}, and a_{ij} are the response coefficient. x_i and x_j are the independent variables, and ε is the associated error. The minimum dilution indicates the least penetration for prior tracks or substrate. CCD RSM is operated to minimize the dilution.

Hence, the dilution of the actual values for the three processing parameters is predicted by the following model:

$$\begin{aligned} dilution = {} & 1.697 - 0.000975P + 0.001v - 0.2104f + 0.00001P{*}P \\ & - 0.000002v{*}v + 0.00518f{*}f - 0.00000P{*}v \\ & + 0.000006P{*}f + 0.000261v{*}f \end{aligned} \quad (2)$$

The analysis of the reduced quadratic model in terms of dilution is shown in Table 2, which shows standard deviation to ensure the reliability of the mathematical model. The F-value is the test statistic used to determine whether the term is associated with the response. P-value is a probability that measures statistical significance. The F-value of the model is 15.22 and the P-value of the model is less than 0.05, which indicates the model terms are significant. The model terms of f, the second order $f{*}f$, and the interactive $v{*}f$ are all significant in the model. Among others, the coefficient of f is 0.2104, which indicates that the feed rate has the largest effect on the response dilution. The statistics R^2 is 0.932, suggesting a good fitting between the predictors and response variable. Fig. 3 shows the model adequacy of the residual plots for dilution. Normal probability plot of the residuals is used to verify the assumption that the residuals are normally distributed. The normal probability plot of the residuals in Fig. 3a approximately follows a straight line with no point deviating the line. The residual against the fitted value in Fig. 3b shows a random distribution with no obvious dispersion pattern. Both demonstrate good adequacy of dilution model [25]. The parametric contributions of first order P, v, and f to the track dilution are 38.3%, 9.1%, and 40.1%, which suggests the main dependence on the f and P.

Fig. 4 shows the contour and surface plots of dilution at constant , v, or f, respectively. At a constant of P of 1500W, the darkest blue region in Fig. 4a represents the minimum

Table 2 – Analysis of variance (ANOVA) for track dilution. (DF: Degree of freedom; Adj SS: Adjusted sums of squares; Adj MS: Adjusted mean squares; S: Standard deviation of the distance between the data values and the fitted values; R^2: the percentage of variation in the response.)

Source	DF	Adj SS	Adj MS	F-value	P-Value
Model	9	0.034291	0.003810	15.22	0.000
Linear	3	0.008841	0.002947	11.77	0.001
P	1	0.003386	0.003386	13.52	0.004
v	1	0.000808	0.000808	3.23	0.103
f	1	0.003548	0.003548	14.17	0.004
Square	3	0.007895	0.002632	10.51	0.002
P*P	1	0.004629	0.004629	18.49	0.002
v * v	1	0.001816	0.001816	7.25	0.023
f* f	1	0.000216	0.000216	0.86	0.375
2-way interaction	3	0.011941	0.003980	15.90	0.000
P* v	1	0.000923	0.000923	3.69	0.084
P* f	1	0.000032	0.000032	0.13	0.729
v* f	1	0.009712	0.009712	38.79	0.000
Error	10	0.002504	0.000250		
Total	19	0.036795			
S			R^2	R^2 (adj)	R^2 (pre)
0.0158234			93.20%	87.07%	59.23%

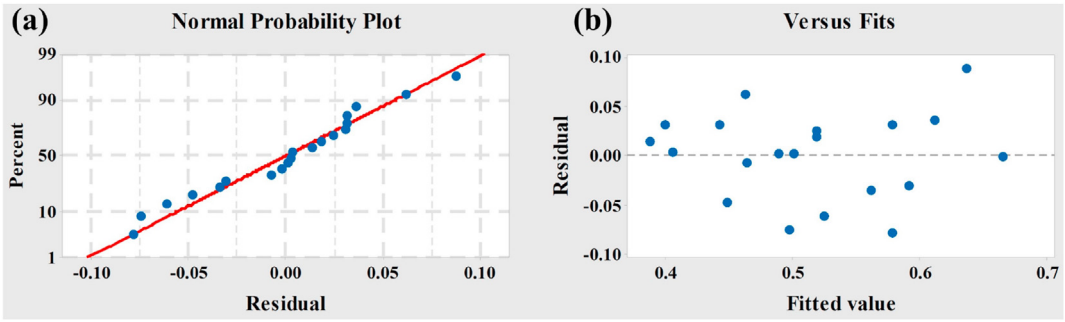

Fig. 3 – Residual plots for dilution. (a) Normal probability plot and (b) residual vs fitted value plot.

dilution, corresponding to the lowest value in Fig. 4d. The lightest green regions in Fig. 4b and c also indicate the minimum dilution. Fig. 4e shows that a higher f within a certain range of P is beneficial to obtain a smaller value at a constant v of 360 mm/min. As shown in Fig. 4f, minimum dilution is achieved at a lower v at a constant f of 6 g/min.

3.2. *Determination of optimal processing parameters*

Therefore, the optimal LMD processing parametric combination can be achieved with the aim of minimum dilution by RSM and the most desirable operation equation can be given:

$$Desirability = \left[\prod_{i=1}^{N} d_i^{r_i}\right]^{1/\sum r_i} \quad (3)$$

where N is the number of responses, d_i and r_i represent the importance and partial desirability function for a specific response, respectively. The desirability function would satisfy all responses with a high or low limit of requirement [12]. The optimal processing parameters can be determined under the aim of minimum dilution. Fig. 5 suggests that the optimal laser power is 1442 W with the scanning speed of 360 mm/min and a feed rate of 6 g/min. Owing to that the laser power is slightly increased in compensation for the ceramic addition, the optimal parameters (1500W, 360 mm/min, 6 g/min) are used for the subsequent fabrication of the composites.

4. Result and discussion

4.1. *Microstructure of TMCs*

Fig. 6 shows the microstructures of TMCs samples with different processing parameters and compositions. The microstructures of TMC0 with inferior parameters (1800 W, 360 mm/min, and 4.8 g/min) and optimal parameters (1500W, 360 mm/min, 6 g/min) are observed in Fig. 6a–b. The two optical images show similar morphology of columnar β grains, growing along the building direction due to large melting dilution to the underlying layer. For titanium-based alloys, the length of columnar grains generally depends on single track while the width is subject to solidification conditions. The columnar width is regarded as the evaluation factor of the β-Ti of the LMD process [26]. Here, the average columnar width reduces from 425 to 286 μm as the parameters change, indicating that parameter optimization plays an important role in grain refinement. Wang et al. [13] studied the effect of mass deposition rate on the microstructure of TC11 alloy and they found that it was effective to control the microstructure

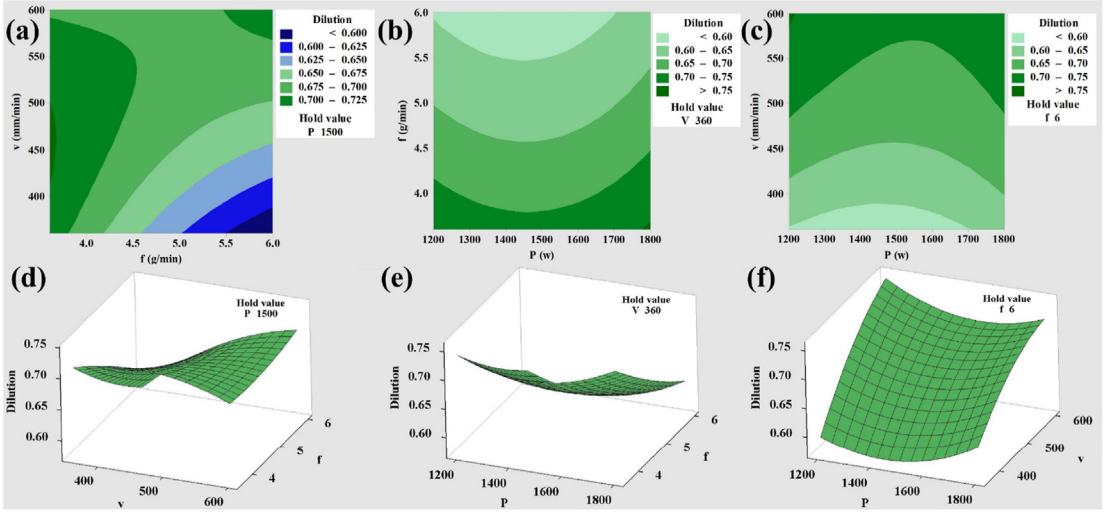

Fig. 4 – Contour and surface plots of dilution vs (a, d) v and f with constant P; (b, e) P and f at constant v; (c, f) P and v at constant f.

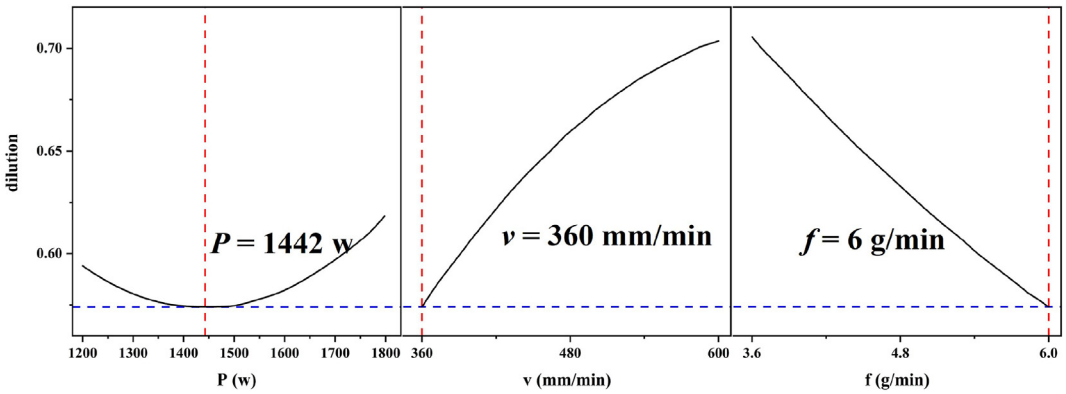

Fig. 5 – Optimizing processing parameters of P, *v* and *f* with minimum dilution.

morphology by adjusting the processing parameters. However, it is difficult to obtain fully equiaxed grains by solely optimizing processing parameters to alter the high cooling rate and temperature gradient ahead of the solid-liquid interface.

With the addition of TiB_2 and La_2O_3, the microstructure of TMC1 and TMC2 become obviously refined with the transition from columnar to equiaxed grains in Fig. 6d–c. According to the in-situ reaction of $Ti + TiB_2 \rightarrow 2TiB$, the formation of in-situ TiB for TMC1 and TMC2 can be calculated with the theoretical volume fraction of 5.04 and 8.33 vol% respectively. As shown in Fig. 6c, the structure of TMC1 is tailored by the discontinuous grain boundaries, referring to a three-dimension quasi-continuous network structure (3DQCN) [22]. For TMC2, the grain boundaries are more continuous and apparent than that

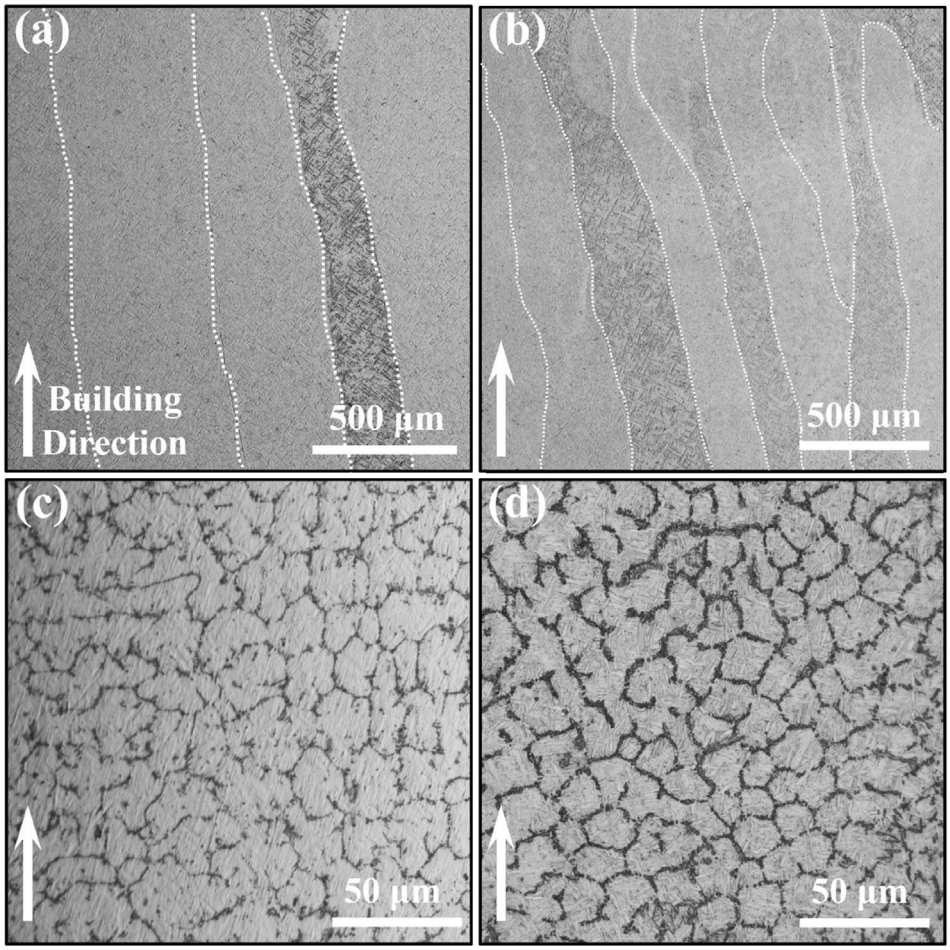

Fig. 6 – Optical images of (a)TMC0 fabricated by inferior processing parameter (1800 W, 360 mm/min, and 4.8 g/min); (b) TMC0, (c) TMC1 and (d) TMC2 fabricated by optimal parameters (1500W, 360 mm/min, 6 g/min). All the following results are obtained on TMCs fabricated by the optimal parameters. The white arrow represents the building direction.

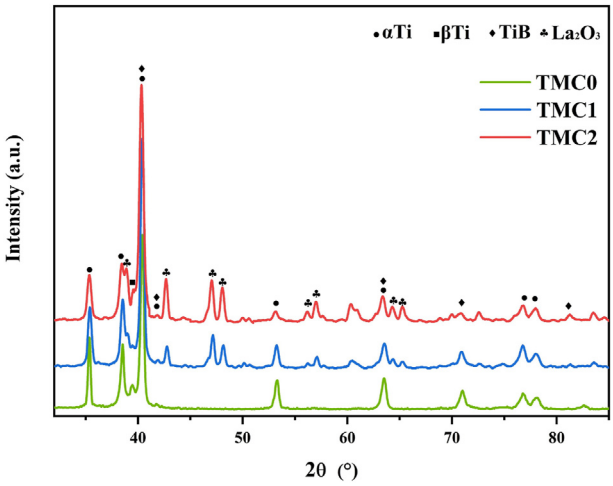

Fig. 7 – XRD patterns of TMC0, TMC1, and TMC2.

of TMC1. The grain size effectively decreases to 23.3 and further 11.9 μm for TMC1 and TMC2, implying that the grain refinement is closely related to the manipulation of both processing parameters and the addition of reinforcements.

4.2. *Phase characterization*

In-situ reinforcements are significant for microstructure evolution and mechanical performance. The phase formation analysis is measured for the TMCs after deposition. Fig. 7 shows the XRD patterns of TMC0, TMC1, and TMC2. The profile of TMC0 reveals the typical phases of α (a = 2.9406 Å, c = 4.67 Å) and β (c = 3.32 Å). There is a weak (110) peak of bcc phase at 39.4°, indicating a small amount of retained β phase. The diffraction peaks of TiB with B27 space group (lattice parameter of a = 6.12 Å, b = 3.06 Å, and c = 4.56 Å) are exhibited in XRD profiles of TMC1 and TMC2, demonstrating that the in-situ reaction between TiB_2 and Ti occurs and TiB is synthesized in the melting pools. Furthermore, the diffraction peaks of La_2O_3 reinforcements also appear compared to that of TMC0. The morphology and microstructure of TiB and La_2O_3 are identified by further TEM results.

Fig. 8a–b exhibits the longitudinal nano-TiB rod growing along [010] direction and the TiB cross section with (100) plane. It is also verified by SAED patterns with the zone axis of [010] in Fig. 8c. The interplanar spacing of $(110)_\beta$ and $(200)_{TiB}$ are 2.33 and 3.1 Å that reveals the $[010]_{TiB}//[-111]_\beta$ orientation relationship between β and TiB in Fig. 8d. Fig. 8e–g presents the nearly spherical nanoparticles of La_2O_3, precipitating in the matrix and the diameter approximately ranges from 125 to 355 nm. Compared with the irregular shapes of raw material in Fig. 1c, La_2O_3 particles becomes spherical after deposition and the size also decreases from micron to nanometer scale. Fig. 8h also verifies the orientation relationship between La_2O_3 and β phase of $(10\bar{1}1)_{La2O3}//(100)_\beta$. The lattice mismatch is calculated to be 5%, which meets a semi-coherent relationship. Besides, La_2O_3 particles can be thermodynamically stable in the titanium melt which is the key requirement for heterogenous nucleation. It reported that the rare earth metal oxides (RE_2O_3) have lower free energies than titanium dioxide [27,28], and is thermodynamically stable not only at titanium freezing temperature, but also under appropriate thermal conditions. Wang et al. [29] studied the mechanism of hierarchical grain refinement of Ti6Al4V by the addition of Y_2O_3 during AM. They found that the primary and secondary Y_2O_3 particles can effectively refine the microstructure during solidification.

4.3. *Microstructure evolutions of titanium matrix*

The detailed SEM images imply the microstructure evolution with the different reinforcement addition. Fig. 9a shows that the duplex phase microstructure of TMC0 consists of the uniform and fine basket-weave α+β matrix. The α laths are bright field and thin layer β phases are dark region as shown in

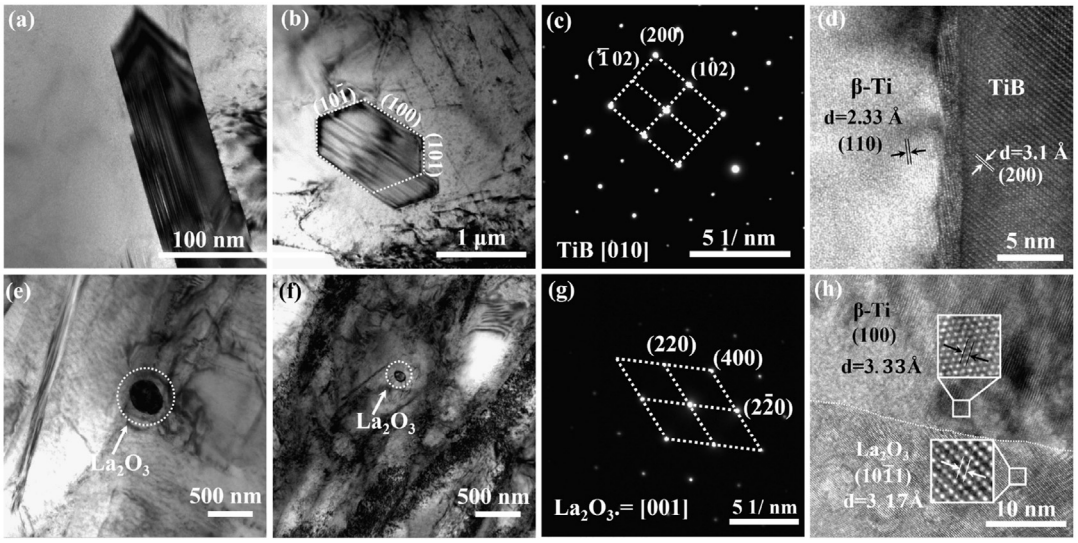

Fig. 8 – TEM characterizations of TMC2. (a, b) Longitudinal and cross section of TiB; (c) SAED pattern of TiB; (d) HRTEM image of β-Ti/TiB boundary; (e, f, and g) La_2O_3 in the titanium matrix; (h) SAED pattern of La_2O_3/β-Ti.

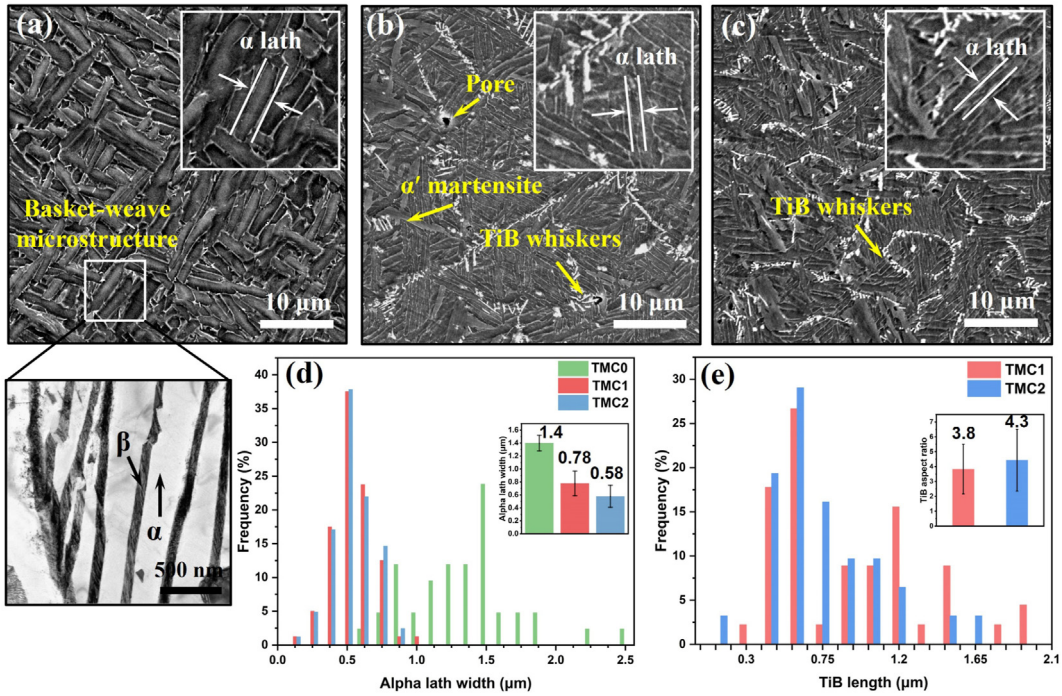

Fig. 9 – SEM images of (a)TMC0 with TEM inset of the Ti6Al4V matrix (α+β phases); (b) TMC1; (c) TMC2. (d) Average α lath width and frequency percent of different samples; (e) average TiB length and frequency percent of TMC1 and TMC2.

TEM inset, which attributes to that Al preferentially partitions to α phase for stabilization while more V enters β phase [4]. V atoms solidly dissolve into Ti matrix and segregated at the interface can slow down the growth of TiB whiskers, as reported by Yang et al. [30]. The growth rate of orthorhombic TiB along the [010] direction is faster than those directions perpendicular to (100), (101), and (001) planes due to the relatively higher density of B–B chains along the [010] direction, leading to needle-like whiskers TiB in the matrix [31,32]. Fig. 9b suggests the in-situ TiB whiskers at grain boundaries that tailor coarse columnar to 3DQCN structure in Fig. 6c–d, as the similar result reported by Huang et al. [14]. The residual α′ phase is observed in the titanium matrix. During the LMD solidification process with cooling rates in a range of 10^3–10^5 °C/s, martensitic α′ forms (β→α′) when the martensite start temperature is 800 °C and critical cooling rate exceeds 410 °C/s [4]. α′ phase can decompose into α and β phases at a temperature of 650 °C [33]. It also shows the pores caused by deflects of raw Ti6Al4V powder or an insufficient melting around the interface between in-fill hatch and contour. With the generation of more in-situ TiB whiskers, Fig. 9d shows the finer grain size of TMC2. The influence of reinforcement addition on Ti matrix microstructures is shown in Fig. 9d–e. The average α lath width decreases from 1.4 to 0.58 μm and the average TiB length increases from 3.8 to 4.3 μm. The increase of TiB length is not significant with increasing volume fraction of TiB.

Hill et al. [34] reported that TiB is the potent heterogenous nucleation site and facilitates α phase nucleation. The equiaxed α grains nucleate and grow from the TiB precipitates at lower cooling rate while the α phase precipitates form the Widmanstätten lath-like morphology under a faster cooling rate. Cui et al. [28] also reported that the cooling rate of Ti6242S–1B fabricated by AM mainly ranges between 10^4 and 10^6 °C/s, and it is inclined to form a finer α phase. Here 8.33 vol % TiB whiskers in TMC2 may provide more sites for nucleation, leading to the reduction of α lath width. La_2O_3 particles also play an important role in microstructure evolution. Yang et al. [35] studied the effects of La_2B_6 on the microstructure and mechanical properties prepared by powder metallurgy. They found that La_2O_3 particles dispersed throughout the matrix and the average length and aspect ratio decreased with

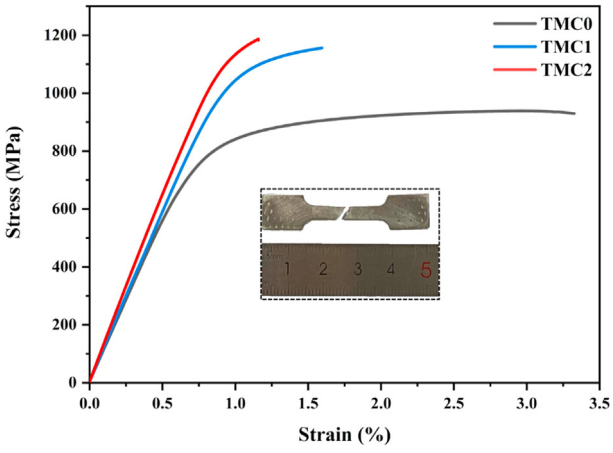

Fig. 10 – Stress-strain curve of TMC0, TMC1, and TMC2 with tensile sample after fracture of TMC2.

Table 3 – Stress-strain behavior of TMCs.

Samples	Ultimate tensile strength (MPa)	Yield strength (MPa)	Elongation (%)
TMC0	938	820	3.4
TMC1	1122	1098	1.2
TMC2	1186	1161	1.1

significant microstructural refinement. It can conclude that under extreme solidification conditions pinning of TiB and La_2O_3 lead to refinement in the titanium matrix.

4.4. *Grain and microstructure refinement mechanism*

Grain morphology is closely associated with the thermal conditions during the layer-by-layer deposition process. Improper processing parameters may induce large dilution, large melting penetration to the underlying layer, and high temperature gradient ahead of the liquid/solid interface. Fan et al. [36] studied the microstructural control of Ti6Al4V manufactured by AM integrated with synchronous induction heating. They proposed that the width of β grain and α lath can be in-situ controlled by optimizing the laser induction parameters. However, the optimization of parameters plays a limited effect on the solidification of a small melting pool. Secondly, in-situ TiB and La_2O_3 have a semi-coherent interface and small mismatch with the Ti matrix, as shown in Fig. 8. According to the Ti–B binary phase diagram [37], the liquid transforms to β and TiB at 1540 °C and transformation of β to α occurs at 884 °C. The precipitated TiB whisker can pin on the boundaries of prior β grains and form 3DQCN structure, which facilitates heterogenous nucleation and grain refinement. Thirdly, constitutional supercooling, controlled by the inherent nature of solute and titanium, is essential for equiaxed grains. The alloy solute plays an important role in the generation of constitutional supercooling which is determined by the growth restriction factor (Q). When new grains coarse into the liquid metal, Q is a measure of the growth restricting effect of solute elements on the growth of the solid-liquid interface of the grains [38]. The solutes with higher Q value are easier to generate larger constitutional supercooling and effectively realize grain refinement. Al and V have negligible Q in Ti [39], indicating it hardly obtains refine microstructure in AM process. While

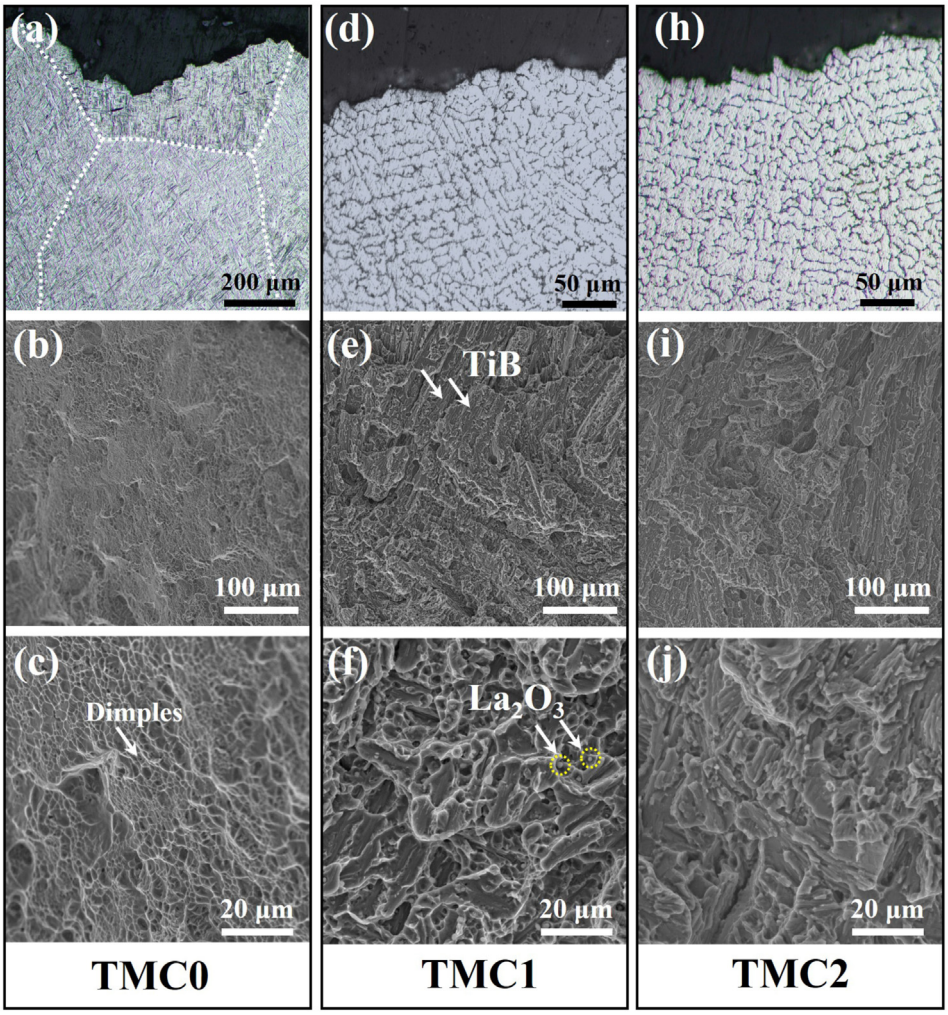

Fig. 11 – Optical images of crack propagation and SEM images of fracture surfaces with low and high magnifications for (a–c) TMC0; (d–f) TMC1; (h–j) TMC2.

the calculated Q for B and La elements in Ti are 66 c_0 and 3.3 c_0 (c_0 is defined as initial concentration in wt.%), respectively [40]. Therefore, the coupling (TiB + La_2O_3) reinforcements can act as potent nucleation agents to promote heterogeneous nucleation and provide constitutional undercooling to promote the CET.

4.5. *Mechanical performance and strengthening mechanism*

Fig. 10 displays the stress-strain curves and the fractured tensile sample of TMC2. The ultimate tensile strengths (UTS), yield strength (YS), and elongations are listed in Table 3. YS of TMCs increases from 820 to 1161 MPa with the loss of elongation. The UTS of TMC1 and TMC2 increased by 19.6% and 26.4% compared to TMC0 due to the strengthening effect of coupling reinforcements.

As shown in Fig. 11a–c, the tensile sample of TMC0 depicts the transgranular fracture with cracks propagating across the coarse columnar grains (highlighted by white dash lines). The fracture surface is characterized with ductile dimples, indicating better ductility and lower tensile strength than TMC1 and TMC2. The optical microstructure of TMC1 exhibits intergranular fracture along the TiB-rich grain boundary. The fractured TiB whiskers and rough bulges are observed in Fig. 11e. Fig. 11f also displays small dimples in which there are La_2O_3 particles in the Ti6Al4V matrix because insufficient TiB whiskers is unable to enclose refined grains. TMC2 also shows the intergranular fracture, as shown in Fig. 11i–j.

The increase of yield strength is caused by existence of TiB whiskers, grain refinement, and the presence of La_2O_3. The increment of yield strength by TiB can be given as [41]:

$$\Delta\sigma_{TiB} = 0.5\sigma_{matrix} V_{TiB}\left(\frac{l_{TiB}}{d_{TiB}}\right)C_0 \quad (4)$$

where σ_{matrix} is the yield strength of Ti6Al4V, V_{TiB} is the volume fraction of TiB, l_{TiB} is the average length of TiB, d_{TiB} is the average diameter of TiB, and C_0 is the orientation factor and equal to 0.125 due to the random array model. It shows that the increment of yield strength increases with the larger volume faction of TiB. The increment of grain refinement and Orowan strengthening can be given as [42,43]:

$$\Delta\sigma_{hall-petch} = k_y(d_m)^{-0.5} - k_y(d_r)^{-0.5} \quad (5)$$

$$\Delta\sigma_{Orowan} = \frac{0.13G_m b}{d_{La2O3}\left(\frac{1}{2V}\right)\frac{1}{3} - d_{La2O3}}\ln\left(\frac{d_{La2O3}}{2b}\right) \quad (6)$$

where k_y is the strengthening constant, d_m is the α thickness of in Ti6Al4V composite and d_r is the α thickness in Ti6Al4V composite with reinforcements. G_m is the shear modulus, b is the Burgers vector, d_{La2O3} is the particle size and V is the volume fraction of La_2O_3. The thickness of α lath in Fig. 9d decreases from 1.4 to 0.58 μm, indicating the increasing yield strength of the composites. The superior strengthening effect is mainly attributed to the increased reinforcement connectivity in the network boundary and the strong interfacial bonding between the reinforcement and matrix, as shown in Fig. 8.

5. Conclusion

In this study, the optimal processing parameters were determined based on the central composite design (CCD) of response surface methodology (RSM) experimental data of single tracks. In-situ (TiB + La_2O_3)/Ti6Al4V composites were built by feeding the Ti6Al4V powder covered by TiB_2 and La_2O_3 powder. The microstructure evolution, phase constitution, and mechanical properties of the components were studied. The main conclusions were obtained as follows.

(1) The optimized processing parameter set ensures the minimum dilution through RSM CCD analysis. The parameter optimization effectively reduces the width of prior β grains.
(2) The microstructure of pure Ti6Al4V is the epitaxial grain growth with coarse columnar grains. With the addition of TiB_2 and La_2O_3, the equiaxed grains were obtained with the grain sizes decreasing dramatically.
(3) In-situ TiB and La_2O_3 are potent heterogenous nucleation particles with specific orientation relationships for titanium. Besides, B and La elements provide large constitutional supercooling that is essential for equiaxed grains.
(4) The ultimate tensile strength of (3 wt% TiB_2+0.5 wt% La_2O_3)/Ti6Al4V and (5 wt% TiB_2+0.5 wt% La_2O_3)/Ti6Al4V increased by 19.6% and 26.4% compared to that of Ti6Al4V. The reinforcements acting as grain boundaries can blunt and deflect cracks, slow crack propagation, and bear the strain.

Declaration of competing interest

The authors declare that they have no known competing financial interests or personal relationships that could have appeared to influence the work reported in this paper.

Acknowledgement

The authors are grateful for funding from the Natural Science Foundation of China (52274401).

REFERENCES

[1] DebRoy T, Mukherjee T, Milewski J, Elmer J, Ribic B, Blecher J, et al. Scientific, technological and economic issues in metal printing and their solutions. Nat Mater 2019;18(10):1026–32.
[2] Gong G, Ye J, Chi Y, Zhao Z, Wang Z, Xia G, et al. Research status of laser additive manufacturing for metal: a review. J Mater Res Technol 2021;15:855–84.
[3] Zhang D, Sun S, Qiu D, Gibson MA, Dargusch MS, Brandt M, et al. Metal alloys for fusion-based additive manufacturing. Adv Eng Mater 2018;20(5):1700952.

[4] Tan X, Kok Y, Tan YJ, Descoins M, Mangelinck D, Tor SB, et al. Graded microstructure and mechanical properties of additive manufactured Ti–6Al–4V via electron beam melting. Acta Mater 2015;97:1–16.
[5] Kok Y, Tan XP, Wang P, Nai M, Loh NH, Liu E, et al. Anisotropy and heterogeneity of microstructure and mechanical properties in metal additive manufacturing: a critical review. Mater Des 2018;139:565–86.
[6] Murr L. Metallurgy principles applied to powder bed fusion 3D printing/additive manufacturing of personalized and optimized metal and alloy biomedical implants: an overview. J Mater Res Technol 2020;9(1):1087–103.
[7] Li N, Cui C, Liu S, Liu S, Cui S, Wang Q. Microstructure and mechanical properties of Ti6Al4V alloy modified and reinforced by in situ Ti5Si3/Ti composite ribbon inoculants. Metals 2017;7(7):267.
[8] Nartu MSKKY, Mantri SA, Pantawane MV, Ho Y-H, McWilliams B, Cho K, et al. In situ reactions during direct laser deposition of Ti-B4C composites. Scripta Mater 2020;183:28–32.
[9] Chen Y, Yang C, Fan C, Zhuo Y, Lin S, Chen C. Grain refinement of additive manufactured Ti-6.5 Al-3.5 Mo-1.5 Zr-0.3 Si titanium alloy by the addition of La2O3. Mater Lett 2020;275:128170.
[10] Hong C, Gu D, Dai D, Alkhayat M, Urban W, Yuan P, et al. Laser additive manufacturing of ultrafine TiC particle reinforced Inconel 625 based composite parts: tailored microstructures and enhanced performance. Mater Sci Eng, A 2015;635:118–28.
[11] Hofman J, De Lange D, Pathiraj B, Meijer J. FEM modeling and experimental verification for dilution control in laser cladding. J Mater Process Technol 2011;211(2):187–96.
[12] Sun Y, Hao MJO. Statistical analysis and optimization of process parameters in Ti6Al4V laser cladding using Nd: YAG laser. Opt Laser Eng 2012;50(7):985–95.
[13] Wang T, Zhu YY, Zhang SQ, Tang HB, Wang HM. Grain morphology evolution behavior of titanium alloy components during laser melting deposition additive manufacturing. J Alloys Compd 2015;632:505–13.
[14] Huang LJ, Geng L, Li AB, Yang FY, Peng HX. In situ TiBw/Ti–6Al–4V composites with novel reinforcement architecture fabricated by reaction hot pressing. Scripta Mater 2009;60(11):996–9.
[15] Traxel KD, Bandyopadhyay A. Influence of in situ ceramic reinforcement towards tailoring titanium matrix composites using laser-based additive manufacturing. Addit Manuf 2020;31.
[16] Hayat MD, Singh H, He Z, Cao P. Titanium metal matrix composites: an overview. Compos Part A 2019;121:418–38.
[17] Du B, Paital SR, Dahotre NB. Synthesis of TiB_2–TiC/Fe nano-composite coating by laser surface engineering. Opt Laser Technol 2013;45:647–53.
[18] Li N, Liu W, Xiong H, Qin R, Huang S, Zhang G, et al. In-situ reaction of Ti-Si-C composite powder and formation mechanism of laser deposited Ti6Al4V/(TiC+Ti_3SiC_2) system functionally graded material. Mater Des 2019;183:108155.
[19] Pouzet S, Peyre P, Gorny C, Castelnau O, Baudin T, Brisset F, et al. Additive layer manufacturing of titanium matrix composites using the direct metal deposition laser process. Mater Sci Eng, A 2016;677:171–81.
[20] Hu Y, Cong W, Wang X, Li Y, Ning F, Wang H. Laser deposition-additive manufacturing of TiB-Ti composites with novel three-dimensional quasi-continuous network microstructure: effects on strengthening and toughening. Compos Part B 2018;133:91–100.
[21] Tjong SC, Ma ZY. Microstructural and mechanical characteristics of in situ metal matrix composites. Mater Sci Eng R 2000;29(3–4):49–113.
[22] Cai C, Radoslaw C, Zhang J, Yan Q, Wen S, Song B, et al. In-situ preparation and formation of TiB/Ti-6Al-4V nanocomposite via laser additive manufacturing: microstructure evolution and tribological behavior. Powder Technol 2019;342:73–84.
[23] Bermingham MJ, StJohn DH, Krynen J, Tedman-Jones S, Dargusch MS. Promoting the columnar to equiaxed transition and grain refinement of titanium alloys during additive manufacturing. Acta Mater 2019;168:261–74.
[24] Chelladurai SJS, Murugan K, Ray AP, Upadhyaya M, Narasimharaj V, Gnanasekaran S. Optimization of process parameters using response surface methodology: a review. Mater Today 2021;37:1301–4.
[25] Bhardwaj T, Shukla M, Paul CP, Bindra KS. Direct energy deposition - laser additive manufacturing of titanium-molybdenum alloy: parametric studies, microstructure and mechanical properties. J Alloys Compd 2019;787:1238–48.
[26] Zhao Z, Chen J, Lu X, Tan H, Lin X, Huang W. Formation mechanism of the α variant and its influence on the tensile properties of laser solid formed Ti-6Al-4V titanium alloy. Mater Sci Eng, A 2017;691:16–24.
[27] Akahori T, Niinomi M, Fukui H, Ogawa M, Toda HJMS. Improvement in fatigue characteristics of newly developed beta type titanium alloy for biomedical applications by thermo-mechanical treatments. Mater Sci Eng C 2005;25(3):248–54.
[28] Cui Y, Aoyagi K, Zhao Y, Yamanaka K, Hayasaka Y, Koizumi Y, et al. Manufacturing of a nanosized TiB strengthened Ti-based alloy via electron beam powder bed fusion. Addit Manuf 2020;36.
[29] Wang X, Zhang L-J, Ning J, Li S, Zhang L-L, Long J. Hierarchical grain refinement during the laser additive manufacturing of Ti-6Al-4V alloys by the addition of micron-sized refractory particles. Addit Manuf 2021;45:101472.
[30] Yang A, Wu Y, Duan Y, Peng M, Zheng S, Li M, et al. The effect of alloying elements in Ti-5Mo-5V-8Cr-3Al alloy on growth kinetics of TiB whiskers in boride layer. Mater Des 2023;225:111478.
[31] Panda K, Chandran KRJAM. First principles determination of elastic constants and chemical bonding of titanium boride (TiB) on the basis of density functional theory. Acta Mater 2006;54(6):1641–57.
[32] Peng M-J, Duan Y-H, Ma L-S, Shu B-P. Characteristics of surface layers on Ti6Al4V alloy borided with CeO2 near the transition temperature. J Alloys Compd 2018;769:1–9.
[33] Mur FG, Rodríguez D, Planell Jjjoa. Influence of tempering temperature and time on the α′-Ti-6Al-4V martensite. J Alloys Compd 1996;234(2):287–9.
[34] Hill D, Banerjee R, Huber D, Tiley J, Fraser H. Formation of equiaxed alpha in TiB reinforced Ti alloy composites. Scripta Mater 2005;52(5):387–92.
[35] Yang YF, Luo S, Qian M. The effect of lanthanum boride on the sintering, sintered microstructure and mechanical properties of titanium and titanium alloys. Mater Sci Eng, A 2014;618:447–55.
[36] Fan W, Tan H, Zhang F, Feng Z, Wang Y, Zhang L-C, et al. Overcoming the limitation of in-situ microstructural control in laser additive manufactured Ti–6Al–4V alloy to enhanced mechanical performance by integration of synchronous induction heating. J Mater Sci Technol 2021;94:32–46.

[37] Ma X, Li C, Du Z, Zhang W. Thermodynamic assessment of the Ti–B system. J Alloys Compd 2004;370(1–2):149–58.
[38] Mitrašinović A, Hernández FR. Determination of the growth restriction factor and grain size for aluminum alloys by a quasi-binary equivalent method. Mater Sci Eng, A 2012;540:63–9.
[39] Bermingham M, McDonald S, Dargusch M, StJohn D. Grain-refinement mechanisms in titanium alloys. J Mater Res 2008;23(1):97–104.
[40] Bermingham MJ, McDonald SD, StJohn DH, Dargusch MS. Beryllium as a grain refiner in titanium alloys. J Alloys Compd 2009;481(1–2):L20–3.
[41] Guo X, Wang L, Wang M, Qin J, Zhang D, Lu W. Effects of degree of deformation on the microstructure, mechanical properties and texture of hybrid-reinforced titanium matrix composites. Acta Mater 2012;60(6–7):2656–67.
[42] Dieter GE, Bacon D. Mechanical metallurgy. New York: McGraw-hill; 1976.
[43] Hayes BJ, Martin BW, Welk B, Kuhr SJ, Ales TK, Brice DA, et al. Predicting tensile properties of Ti-6Al-4V produced via directed energy deposition. Acta Mater 2017; 133:120–33.